Materials Advances

ROYAL SOCIETY OF CHEMISTRY

PAPER

View Article Online
View Journal | View Issue

Cite this: *Mater. Adv.*, 2025, 6, 6907

Lanthanide-based UCNPs: toxicity evaluation and interaction of ultrasmall core *vs.* core–shell nanoparticles with cells

Mykhailo Nahorniak,[a] Daniel Horák, *[a] Miroslav Šlouf,[a] Miloš Steinhart,[ab] Oleksandr Shapoval,[a] Hana Engstová[c] and Petr Ježek[c]

We describe a new concept for preparation of ultrasmall $NaYF_4$:Yb,Er upconversion nanoparticles (UCNPs) with a diameter of 7 nm, depending on the amount of water added in the polymerization mixture, which affects the nucleation and growth of the particles. The morphology and structure of the nanoparticles were thoroughly characterized both in the dried state (TEM including elemental analysis and electron diffraction) and in solution (small and wide-angle X-ray scattering and dynamic light scattering). A thick $NaYF_4$ shell was subsequently introduced onto the particles, which significantly increased the luminescence by minimizing surface quenching effects and passivating the core from the surrounding environment. To make the particles dispersible in the aqueous environment natural for biological applications, they were coated with a ~6 nm thick hydrophilic silica layer. This increased the size of core and core–shell UCNPs to 20 and ~50 nm. All the developed particles exhibited non-cytotoxicity tested in insulinoma INS-1E cells. The upconversion luminescence of these nanoparticles incubated with INS-1E cells showed a similar pattern to that of the particles themselves. The small biocompatible UCNPs developed in this study are promising candidates for non-invasive and non-destructive applications in bioimaging. Thanks to their advantageous properties, *i.e.*, small size, adjustable optical properties and ability to interact with and easily penetrate cells, they are suitable for future use in platforms for targeted drug delivery and advanced diagnostic technologies.

Received 26th May 2025,
Accepted 19th August 2025

DOI: 10.1039/d5ma00542f

rsc.li/materials-advances

Introduction

Recently, interest in upconversion nanoparticles (UCNPs) has been significantly growing due to their widespread use in engineering and biomedical applications,[1] and a number of various reviews have addressed different strategies for their synthesis and emission control.[2] While engineering applications include upconversion nanothermometry (*e.g.*, temperature measurement in batteries),[3] light emitting diodes,[4] photocatalysts,[5] nanofluidics,[6] anti-counterfeiting,[7] superconductors in photovoltaics,[8] solar energy harvesting or data acquisition,[9] conversion and storage,[10] biomedical applications involve mainly theranostics.[11] Here, diagnostics is based on multimodal real-time bioimaging (computer tomography, MRI and fluorescence)[12] and monitoring cell–cell communication.[13] Examples of therapeutic applications are drug and gene delivery, corneal refractive index modification or photothermal and photodynamic therapy of tumors.[14] In addition, UCNPs are used for biosensing in upconversion-linked immunoassays for detection of nucleic acids,[15] prostate specific antigen, cardiac troponin,[16] bladder cancer, bacteria (*Clostridioides* and *Bordetella pertussis*) and viral infections (SARS). At the same time, intensive research is currently in progress on the use of UCNPs for imaging of the pancreas and diagnostics in diabetology.[17]

The unusual feature of UCNPs based on various lanthanide-doped inorganic nanoparticles, typically 10–100 nm in diameter, lies in their unique lanthanide photon upconversion, where they convert low-energy NIR photons into high-energy visible light with a large anti-Stokes shift (>100 nm). UCNPs thus offer many advantages over conventional luminophores, such as long-term multimodal imaging in biomedical applications with excellent brightness, high signal-to-noise ratio, photostability (nonbleaching), continuity of emission (nonblinking), sharp and tunable emission peaks, lack of overlap with cellular autofluorescence, biocompatibility, no photo damage to living cells by NIR laser irradiation, deep tissue penetration and functionalizability. Several-fold improvement in imaging resolution has recently been achieved by photon avalanche UCNPs.[18] The luminescence,

[a] *Institute of Macromolecular Chemistry, Czech Academy of Sciences, Heyrovského nám. 2, 162 00 Prague 6, Czech Republic. E-mail: horak@imc.cas.cz*
[b] *Institute of Applied Physics and Mathematics, Faculty of Chemical Technology, University of Pardubice, 530 02 Pardubice, Czech Republic*
[c] *Department 75, Institute of Physiology, Czech Academy of Sciences, Vídeňská 1083, 142 20 Prague 4, Czech Republic*

namely emission colors of UCNPs is a major parameter that can be manipulated depending on their elements, composition, crystallinity, size, synthesis method, *etc*.[19] In the synthesis, nucleation and particle growth are affected by reaction temperature and time and the precursor/solvent, Na^+/F^- and solvent (octadec-1-ene)/oleic acid ratios;[20] increasing Na^+ ion concentration typically decreases the size of UCNPs.[21] The brightness is then mainly influenced by the UCNP phase, which can be cubic, hexagonal, tetragonal, orthogonal or in the form of platelets.[22] The crystal structure also depends on the choice of alkali ions.[23] Furthermore, the size of UCNPs is also strongly influenced by the viscosity of the reaction medium.

UCNPs consist of a host (oxides, fluorides, chlorides, vanadates), sensitizers such as Yb^{3+} and Nd^{3+} ions that are the energy donors, and activators, *e.g.*, Er^{3+}, Tm^{3+}, Ho^{3+}, Eu^{3+}, Tb^{3+}, Dy^{3+}, Sm^{3+} and Pr^{3+} ions, the energy acceptors.[24] While the selection of dopants tunes the chromacity, optimum upconversion luminescence can be achieved by a short donor–acceptor pair distance (<10 nm)[25] and an optimal rare earth ion ratio.[26] If the particles are doped with gadolinium, they also have magnetic properties.[27] To further enhance the upconversion photoluminescence intensity and quantum efficiency, inert inorganic shells (typically $NaYF_4$, $NaGdF_4$ or CaF_2) are introduced on the core UCNPs to passivate the surface, reduce its radiative quenching and increase the light-harvesting capacity, brightness and quantum yield. The (multi)shell on core UCNPs is typically synthesized by epitaxial growth method using molecular precursors or small sacrificed nanoparticles. However, with increasing UCNP size, the surface-to-volume ratio decreases.

To achieve reproducible results, good performance and at the same time high cell penetration, monodisperse ultrasmall (<10 nm) nanoparticles are required, which are difficult to prepare.[28] Core UCNPs are typically synthesized by coprecipitation of lanthanide chlorides, thermal decomposition of lanthanide trifluoroacetates or oleates at high temperature (>300 °C) or sol–gel synthesis.[21] Also, microwave-assisted synthesis has recently become popular as it is fast, reproducible and allows phase and size control.[29] However, because core UCNPs are prepared in organic solvents and stabilized with hydrophobic ligands (typically oleic acid),[30] they are not dispersible in aqueous media. Another disadvantage of UCNPs is the leakage of lanthanide and fluoride ions into the aqueous environment, potentially causing toxicity and luminescence deterioration.[31] Therefore, it is necessary to modify the UCNP surface with a protective polymer coating to suppress ion leakage and to ensure good dispersibility of the particles in water and colloidal and chemical stability (biocompatibility) characterized by a low solubility product constant. Last but not least, the polymer coating should allow functionalization and thus bioconjugation of various target biomolecules. Various coating chemistries have been therefore developed to introduce biocompatible hydrophobic or hydrophilic polymers with reactive functional groups for conjugation of photoactive biomolecules such as hypericin, rhodamine B, phthalocyanine, Rose Bengal, riboflavin, organic dyes, *etc*. While the hydrophobic polystyrene or poly(methyl methacrylate) coating suppresses the chemical degradation of UCNPs in phosphate buffers,[30] the frequently used hydrophilic poly(acrylic acid) provides good dispersibility and a large number of surface carboxylate groups.[32] Other coatings include biocompatible Federal Drug Administration-approved compounds, such as silica, gum arabic, polyvinylpyrrolidone and poly(ethylene glycol) derivatives.[33,34] Even polyethylenimine, poly(sodium 4-styrene sulfonate), poly(maleic anhydride-*alt*-1-octadecene)[35] and poly(methyl vinyl ether-*alt*-maleic acid) were suggested as coating materials.[36]

Despite the considerable potential of UCNPs in various technological and biomedical applications, their biosafety and biocompatibility have not yet been thoroughly investigated. The interactions of these nanoparticles with biological systems are governed by a number of physicochemical parameters, including chemical composition, particle size and shape, surface charge, and surface functionalization.[37] In particular, the leakage of ions such as lanthanides and fluorides has been associated with oxidative stress, mitochondrial dysfunction, and subsequent cell damage.[38] Furthermore, the potential for long-term accumulation in major organs and the induction of immune responses raises additional safety concerns. In addition, the route of administration plays a key role in determining biodistribution and systemic effects. Therefore, precise surface engineering is essential to mitigate undesirable biological interactions. In this study, silica shell was used as the surface coating due to its well-documented biocompatibility, chemical inertness, and suitability for further functionalization.[39]

The aim of this report was to develop ultrasmall UCNPs with high brightness that would be dispersible in aqueous milieu and safe for biological use.

Experimental

Materials

Erbium(III) chloride hexahydrate (99.9%), anhydrous yttrium(III) (99.99%) and ytterbium(III) chlorides (99.9%), sodium hydroxide (99%), ammonium fluoride (99.99%), tetraethyl orthosilicate (TEOS), octadec-1-ene (OD; 90%), and IGEPAL® CO-520 were purchased from Sigma-Aldrich (St. Louis, MO, USA). Oleic acid (OA; 98%) was purchased from Lachema (Brno, Czech Republic). Absolute ethanol was obtained from LachNer (Neratovice, Czech Republic). RMPI 1640 medium was purchased from the Institute of Molecular Genetics (Prague, Czech Republic). Water used in the synthesis was purified on a Milli-Q IQ 7000 system from Millipore (Molsheim, France).

Synthesis of ultrasmall core $NaYF_4$:Yb,Er nanoparticles (C-UCNPs)

The preparation of C-UCNPs was carried out in two steps. The first step involved dissolving lanthanide chlorides, namely YCl_3, $YbCl_3$, $ErCl_3{\cdot}6H_2O$ in a molar ratio of 0.78 : 0.2 : 0.02 in OD (30 mL) and OA (12 mL) in a 100 mL three-necked vessel at 160 °C for 30 min with stirring (350 rpm) and under an Ar atmosphere by modification of an earlier procedure.[40] The reaction mixture was then cooled to 40 °C and a methanolic solution (12 mL) of NaOH (2.5 mmol) and NH_4F (4 mmol) was slowly dropped into the

Table 1 Characterization of particles

	C-UCNP-I	C-UCNP-II	C-UCNP-III	C-UCNP-IV	C-UCNP-V	C-UCNP-VI
Water[a] (wt%)	0	0.7	1.4	2.1	4.2	8.0
D_n (nm)	320	—[b]	8	7	16	25
$Đ$	1.36	—[b]	1.03	1.05	1.34	1.03

[a] Relative to the reaction mixture (OD, OA and water). [b] Impossible to measure; D_n – number-average diameter (TEM), $Đ$ – dispersity (TEM).

solution. To evaporate the methanol and trace water, the temperature was slowly raised to 120 °C which was maintained for 30 min with stirring under an Ar atmosphere. The second step consisted in cooling the reaction mixture to 60 °C in Ar atmosphere, transferring it to an autoclave equipped with a magnetic stirrer and adding varying amounts of water (0–3 mL); the percentage of water in the reaction mixture was given in Table 1, together with the corresponding particle denotation (C-UCNP-I to VI). After closing, the autoclave was heated in an aluminum bath at 310 °C (pressure 2.1 MPa) for 1.5 h with stirring (350 rpm). Then, the reactor was cooled to room temperature (RT) and the resulting C-UCNPs were separated by centrifugation (3460 rcf) for 30 min in a fivefold excess of ethanol and dispersed in hexane.

Synthesis of core–shell $NaYF_4$:Yb,Er@$NaYF_4$ nanoparticles (CS-UCNPs)

The shell around the C-UCNP-IV nanoparticles was synthesized in a Y-oleate solution prepared by dissolving YCl_3 (0.6 mmol) in OD (9 mL) and OA (3.6 mL) at 160 °C for 30 min under stirring (350 rpm) in an Ar atmosphere. After cooling the solution to 40 °C, a dispersion of C-UCNP-IV nanoparticles (300 mg) in hexane, OA (8.4 mL), OD (21 mL) and a methanolic solution (12 mL) of NaOH (2.5 mmol) and NH_4F (4 mmol) were added dropwise. To evaporate the methanol, hexane and water, the reaction mixture was slowly heated to 120 °C and maintained at this temperature for 30 min with stirring (350 rpm) under Ar atmosphere. This was followed by rapid heating to 300 °C for 1.5 h, cooling to RT, dispersing the resulting CS-UCNPs in a fivefold excess of ethanol, centrifugation (3460 rcf) for 30 min and dispersing the particles in hexane. For the cell experiments, the particles were successively centrifuged and washed with an ethanol/hexane mixture (1/2 and 2/1 v/v), ethanol and water/ethanol (1/2 and 2/1 v/v) and immersed in water.

Surface engineering of C-UCNPs and CS-UCNPs with silica

A previously published method was modified to coat C-UCNPs and CS-UCNPs with silica.[41] The particles were first diluted with hexane to a concentration of 2 mg mL^{-1}, IGEPAL® CO-520 (2 mL per 20 mg particles) was then added and the dispersion was sonicated using a Bandelin ultrasonic homogenizer (Berlin, Germany; amplitude 10%). Then, 25% aqueous ammonia (160 μL) was added, the mixture was sonicated for another 20 min at 10% amplitude, TEOS (160 μL) was added, and the mixture was stirred (800 rpm) for 24 h. The resulting C-UCNP@SiO_2 and CS-UCNP@SiO_2 nanoparticles were washed twice with ethanol, three times with ethanol-water mixture with gradually increasing water content until water completely replaced ethanol.

Characterization methods

For ultrastructural analysis of UCNPs by transmission electron microscopy (TEM), a dispersion of UCNPs in hexane was pipetted (2 μL) onto freshly glow-discharged CF400-Cu carbon-coated grid, which was left in air to evaporate the hexane. The UCNPs were analyzed by a Tecnai G2 Spirit TEM (FEI; Brno, Czech Republic) operating at 120 kV. Morphology of the particles was visualized by bright field imaging (TEM/BF) and their number-average diameter (D_n), weight-average diameter (D_w) and dispersity ($Đ = D_w/D_n$) were calculated from at least 300 particles as described in our previous work.[42] The elemental composition was verified by energy-dispersive analysis of X-rays (TEM/EDX) and the crystal structure was analyzed by selected area electron diffraction (TEM/SAED). TEM/SAED patterns were processed and compared with theoretically calculated powder X-ray diffraction patterns (PXRD) using the open-source program package EDIFF.[43] The crystal structures for the diffraction pattern calculation (α-$NaYF_4$ and β-$NaYF_4$) were obtained from freeware Crystallography Open Database (COD).[44] In addition, the UCNPs were visualized in a JEM2100-Plus high resolution transmission electron microscope (HR-TEM; JEOL; Tokyo, Japan) operating at 200 kV with a TemCam–XF416 4K CMOS camera (TVIPS; Gauting, Germany).

Dynamic light scattering (DLS) was used to measure the hydrodynamic diameter (D_h) and size distribution of nanoparticles (polydispersity; *PD*) in hexane or water and ζ-potential in water at 25 °C on a ZEN 3600 Zetasizer Nano Instrument (Malvern Instruments, UK). D_h and *PD* were determined from the intensity-weighted distribution function, which was derived through CONTIN analysis of the correlation function provided by the Malvern software.

The small and wide-angle X-ray scattering (SWAXS) extended the established small angle X-ray scattering (SAXS) method to a wider range of angles. The angles achieved in this case were not as large as those provided by X-ray diffraction instruments. However, all measurements were performed in the same camera under as similar conditions as possible. Usually only the sample to detector distance was varied. This provided important additional information also from the overlap angle region. For SWAXS, a two-pinhole point focusing SAXS instrument Xeuss Pro made by Xenocs (Grenoble, France) was used. The CuKα beam with a wavelength of $\lambda = 0.154$ nm was generated by a low-power Genix3D microsource operating at 50 kV and 0.6 mA. Scattering was observed with a 2D EIGER2 R 500K detector (Dectris; Baden-Dättwil, Switzerland) with 512 × 1028 pixels, each 75 × 75 μm^2 in size at two different sample to detector distances 1 m (SAXS) and 0.1 m (WAXS). The whole system including the windowless detector was evacuated and

each counting took 1 or 2 h. In each setup, the sample to detector distance was calibrated using an Ag behenate standard. Data were azimuth-averaged and adjusted to absolute scale using a glassy carbon standard. After merging the data from these positions, a reliable q interval from 0.05 to 30.0 nm^{-1} was selected; q is the magnitude of the scattering vector $q = 4\pi \sin(\theta)/\lambda$ and θ is half of the scattering angle. The highest scattering angle corresponded approximately to a value of 25° 2θ.

Upconversion luminescence spectra were measured using an FS5 spectrofluorometer equipped with a CW 980 nm laser diode (MDL-III-980-2W) as the excitation source (Edinburgh Instruments, UK). The laser had a maximum power of 2 W and a beam size of 5 × 8 mm^2.

Attenuated total reflectance coupled with Fourier transform infrared (ATR FTIR) spectra were recorded on a Nexus Nicolet 870 IR spectrometer (Madison, WI, USA) coupled with a liquid nitrogen-cooled mercury-cadmium telluride detector and a GoldenGate single-reflection diamond ATR system (Specac; Orpington, UK).

Thermogravimetric analysis (TGA) of the particles from 25 to 500 °C was carried out in air at a heating rate of 10 °C min^{-1} using a PerkinElmer TGA 7 analyzer (Norwalk, CT, USA).

Cell experiments

Insulin-producing glucose-responsive INS-1E cells from X-ray-induced rat insulinomas were purchased from AddexBio (San Diego, CA, USA; No. C0018009).[45] For their culturing, 11 mM glucose with RPMI 1640 medium supplemented with 5% (v/v) fetal calf serum, 10 mM HEPES, 1 mM pyruvate, 50 mM mercaptoethanol, 50 IU mL^{-1} penicillin and streptomycin (50 mg mL^{-1}) were used.

The *in vitro* cytotoxicity of C-UCNP-IV nanoparticles in water was analyzed using a trypan blue exclusion assay (Thermo Fisher Scientific) on INS-1 cells cultured in 11 mM glucose medium at 37 °C for 48 h in a humidified atmosphere with 5% CO_2. This was followed by incubation with C-UCNP-IV nanoparticles (0.01–0.4 mg mL^{-1}) for 24 h and determination of cell viability by staining with 0.4% trypan blue. The percentage of living cells was measured using a Luna II automated cell counter (Logos Biosystems; Gyeonggi-do, South Korea). Cell viability was assessed from five biological replicates, *i.e.*, passages of INS-1E cells.

Confocal microscopic images of INS-1E cells incubated with ligand-free and silica-coated C-UCNPs and CS-UCNPs (0.4 mg mL^{-1}) for 24 h were taken on poly(L-lysine)-coated coverslips using a Leica SP 8 confocal microscope (Wetzlar, Germany) after excitation at 980 nm with a Coherent 170 fs Chameleon pulsed laser of 100 mW power (Coherent; Saxonburg, PA, USA). Bright-field images of the cells were visualized using the same microscope with a 405 nm lamp.

Results and discussion

Effect of water addition on the morphology of core $NaYF_4$:Yb,Er nanoparticles (C-UCNPs)

As mentioned already in the Introduction, the great benefit of upconversion nanoparticles consists in the absence of optical background ensuring high detection sensitivity. However, their morphology, *i.e.*, particle size, shape and crystallinity are strongly dependent on the way of synthesis, ratio of reactants and viscosity of the reaction medium.[46] In this study, core $NaYF_4$:Yb,Er upconversion nanoparticles (C-UCNP-I to C-UCNP-VI) were prepared in a high-boiling solvent (octadec-1-ene) by oleic acid-stabilized high-temperature coprecipitation of lanthanide chlorides with NH_4F and NaOH, the amount of which was kept constant while varying the amount of water added to the reaction mixture (Table 1).

In the absence of water, huge cubic C-UCNP-I nanoparticles (326 nm) with high dispersity ($Đ$ = 1.36) were formed (Fig. 1a).

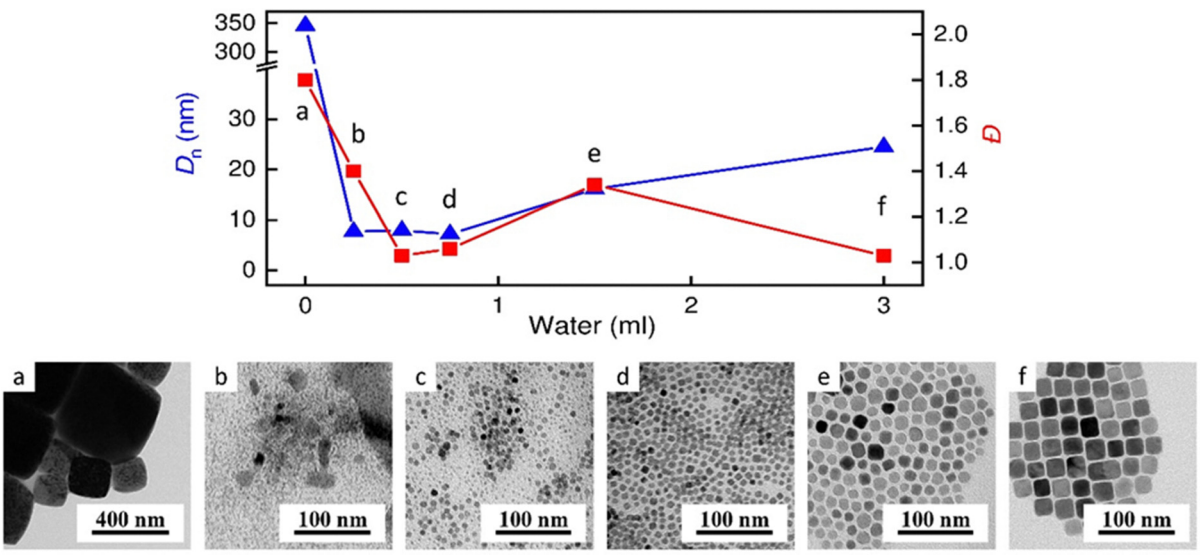

Fig. 1 Dependence of the number-average diameter D_n (triangles) and dispersity $Đ$ (squares) of C-UCNPs on the amount of water in the reaction mixture. (a) C-UCNP-I, (b) C-UCNP-II, (c) C-UCNP-III, (d) C-UCNP-IV, (e) C-UCNP-V, and (f) C-UCNP-VI.

TEM/EDX analysis provided elemental composition roughly corresponding to NaF crystals while TEM/SAED patterns showed that none corresponded to any of the known $NaYF_4$ structures. With the addition of water increasing from 0.7 wt%, the C-UCNP-II particle size and dispersity decreased significantly (Fig. 1b). After the addition of 1.4-2.1 wt% water, the C-UCNP-III and C-UCNP-IV particles were ultrasmall (<10 nm), apparently spherical-like in shape and almost monodisperse ($Đ \leq 1.05$; Fig. 1c and d). This was obviously due to the separation of the nucleation phase from the growth phase, which is a necessary condition for achieving a narrow particle distribution.[47] Such particles will show improved functionality compared to polydisperse ones in optics, medical diagnostics, magnetic resonance imaging and drug delivery; also, in achieving reproducible results. Complete TEM analysis of the smallest (D_n = ~7 nm) and almost monodisperse ($Đ$ ~1.05) C-UNCP-IV nanoparticles documented that they were isomeric (Fig. 2a; Table 2). The TEM/EDX spectra (Fig. 2b) confirmed the expected composition as the dominating peaks corresponded to sodium yttrium fluoride (Na, Y, F) and the remaining peaks (C, Cu) could be attributed to the background because the particles were deposited on a carbon-coated copper grid (Fig. 2a). The TEM/SAED diffraction pattern (Fig. 2c) and its comparison with theoretically calculated PXRD pattern (Fig. 2d) proved that the nanoparticles exhibited the cubic phase of sodium yttrium fluoride – α-$NaYF_4$. The experimental SAED intensities (Fig. 2c; red line) decreased faster with the diffraction vector compared to the theoretically calculated PXRD intensities (Fig. 2c; blue line), which could be attributed to the intrinsic differences between X-ray and electron diffraction and the fact that the crystals were quite small and

Table 2 Characterization of C-UCNP-IV (later denoted as C-UCNPs), C-UCNP@SiO_2, CS-UCNPs, and CS-UCNP@SiO_2 nanoparticles

	D_n (nm)	$Đ$	D_h (nm)	PD	ζ-potential (mV)
C-UCNPs	7	1.05	19[a]	0.14[a]	37
C-UCNP@SiO_2	20	1.04	82[b]	0.20[b]	−23
CS-UCNPs	width: 39	1.01	66[a]	0.19[a]	21
	length: 47	1.00			
CS-UCNP@SiO_2	width: 46	1.02	218[b]	0.16[b]	−23
	length: 55	1.01			

D_n – number-average diameter (TEM), $Đ$ – dispersity (TEM), D_h – hydrodynamic diameter (DLS; [a]in hexane, [b]in water), PD – polydispersity (DLS).

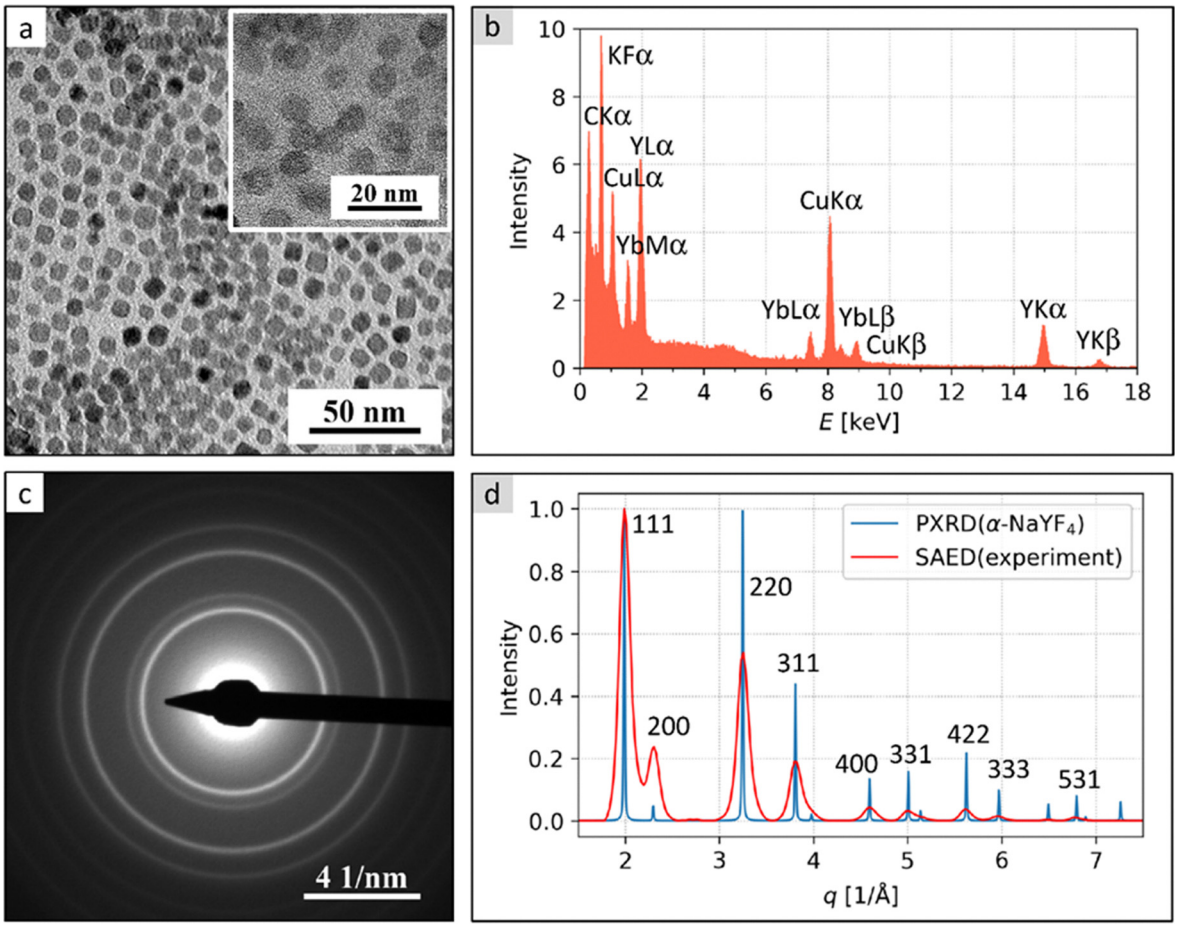

Fig. 2 TEM analysis of C-UCNP-IV particles: (a) TEM/BF micrograph, (b) TEM/EDX spectrum, (c) TEM/SAED diffraction pattern, and (d) comparison of the radially averaged experimental electron diffraction pattern with the theoretically calculated PXRD diffractogram of α-$NaYF_4$. The inset in Figure (a) is obtained at a higher magnification with HRTEM microscope at 200 kV.

their structure exhibited a higher mosaicity, *i.e.*, the degree of misalignment of the crystal lattice planes. The hydrodynamic size of C-UCNP-IV was larger (D_h = 19 nm; *PD* = 0.14) than D_n, which was due to the fact that TEM monitors the sample in the dry compact state, while DLS determines the particles in the solvent-solvated state (Table 2). In addition, TEM measures number-based particle size, whereas DLS distributions are intensity-based (proportional to the power of 6) and are therefore sensitive to the presence of large particles. The ζ-potential of C-UCNP-IV in water (pH = 5.5) was positive (37 mV) due to the cationic nature of lanthanide ions. Such high ζ-potentials are generally associated with colloidally stable systems, while low ζ-potentials indicate low stable colloids.[48]

When 4.2 wt% water was added to the reaction mixture, resulting C-UCNP-V particles consisted of more cubic nanoparticles in addition to spherical ones, according to TEM/BF; their size and dispersity again increased (D_n = 16 nm; $Đ$ = 1.34) compared to C-UCNP-IV (Fig. 1e). On addition of 8 wt% water to the reaction mixture, C-UCNP-VI particles consisted of large irregularly shaped merged crystals of ∼1 μm accompanied by completely cubic particles of 25 nm in size and low dispersity ($Đ$ = 1.03; Fig. 1f). TEM/EDX analysis showed an elemental composition with an unusually high silicon content (probably impurities from synthesis) and TEM/SAED diffraction patterns did not correspond to any of the known $NaYF_4$ structures, similar to the C-UCNP-I.

The size and shape of some synthesized particles in hexane were also analyzed by SWAXS, which can quantify differences in particle scattering density (Fig. 3a). The total scattered X-ray intensity $I(q)$ dependencies showed that the C-UCNP-I and C-UCNP-VI particles were too large to be analyzed by this method. In the region of the smallest accessible angles, log/log $I(q)$ dependencies of these two particle types had a slope of −4 indicating a sharp boundary between particles and the solvent.

But it was not possible to find out more information such as whether the particles were globular, platelets or rods. More information was obtained from measurements of C-UCNP-IV nanoparticles, which could be fitted by a Schulz-Zimm distribution of spheres centered at mean radius $\langle R \rangle$ = 5.1 nm with halfwidth σ = 0.18 and good fit with experimental data documented by R_{factor} = 2.41 (Fig. 3a).

This corresponded quite well to the results from TEM. The particle size distribution measured by SWAX then reflected spherical-like shape of the C-UCNP-IV particles (Fig. 3b). Therefore, only C-UCNP-IV nanoparticles were used in further work, which were hereinafter referred to as C-UCNPs.

Core–shell $NaYF_4$:Yb,Er@$NaYF_4$ nanoparticles (CS-UCNPs)

The disadvantage of ultrasmall UCNPs is that their luminescence is relatively low compared to conventionally sized nanoparticles (D_n = 25 nm). To overcome this shortcoming, a passive $NaYF_4$ shell was introduced on C-UCNPs by injecting its precursors into the reaction mixture. This changed the morphology to rounded and increased the D_n in hexane from 7 nm to 39 nm with a dispersity of 1.01 (Fig. 4; Table 2). At the same time, the D_h increased to 66 nm and the ζ-potential decreased

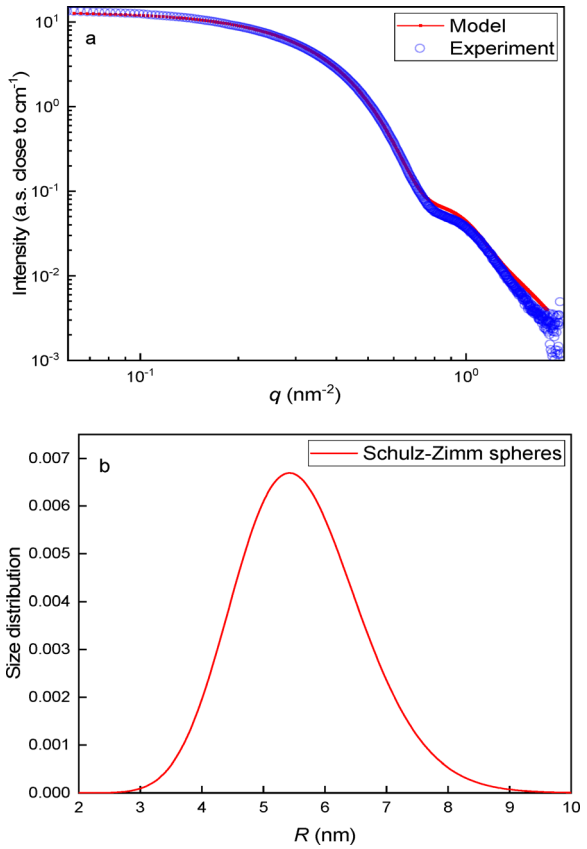

Fig. 3 (a) SWAXS determination of scattered X-ray intensity of C-UCNP-IV nanoparticles and (b) their distribution according to the Schulz-Zimm sphere model.

to 21 mV. This decrease can be attributed to several interrelated factors: (*i*) the increase in particle size due to shell growth affecting the ζ-potential measurements, (*ii*) the shift of the slipping plane (the point where the ζ-potential is measured) from the charged surface lowering apparent ζ-potential, and (*iii*) the composition of the shell. $NaYF_4$ is relatively inert and typically carries negligible surface charge. The introduction of $NaYF_4$ shell onto C-UCNPs substantially increased the luminosity compared to C-UCNPs (Fig. 5a) because the core–shell morphology prevented energy loss during the energy transfer process.[49]

Surface modification of C-UCNPs and CS-UCNPs with silica

C- and CS-UCNPs were hydrophobic due to the presence of OA residues on the particle surface. In order to be colloidally stable in aqueous biological environments, prevent aggregation during storage and reduce potential toxicity, the particles must be coated with a hydrophilic protecting layer such as silica. If the silica is mesoporous, its large surface area allows the introduction of various functional groups or adsorption of pharmaceuticals into the pores, from which they can be released at the target site. Here, the C-UCNPs and CS-UCNPs were encapsulated in dense silica layer by a reverse microemulsion approach with TEOS. Comparison of TEM micrographs of C-UCNPs and

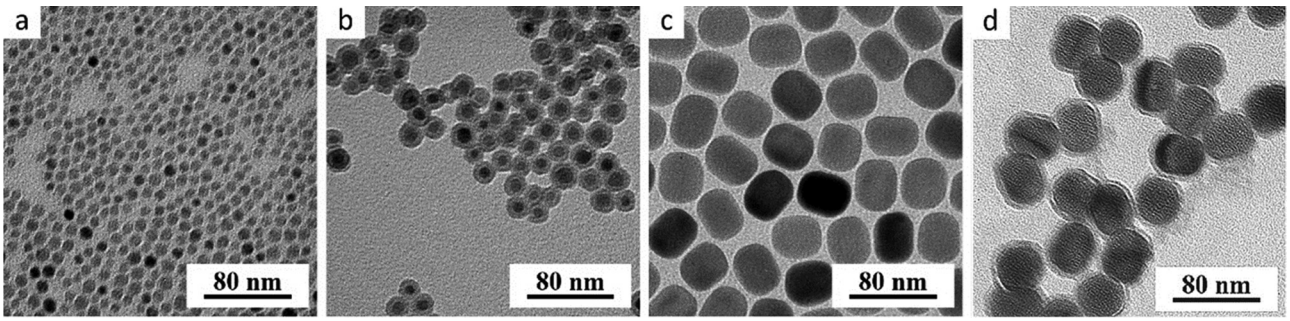

Fig. 4 TEM micrographs of (a) C-UCNPs, (b) C-UCNP@SiO_2, (c) CS-UCNPs, and (d) CS-UCNP@SiO_2 nanoparticles.

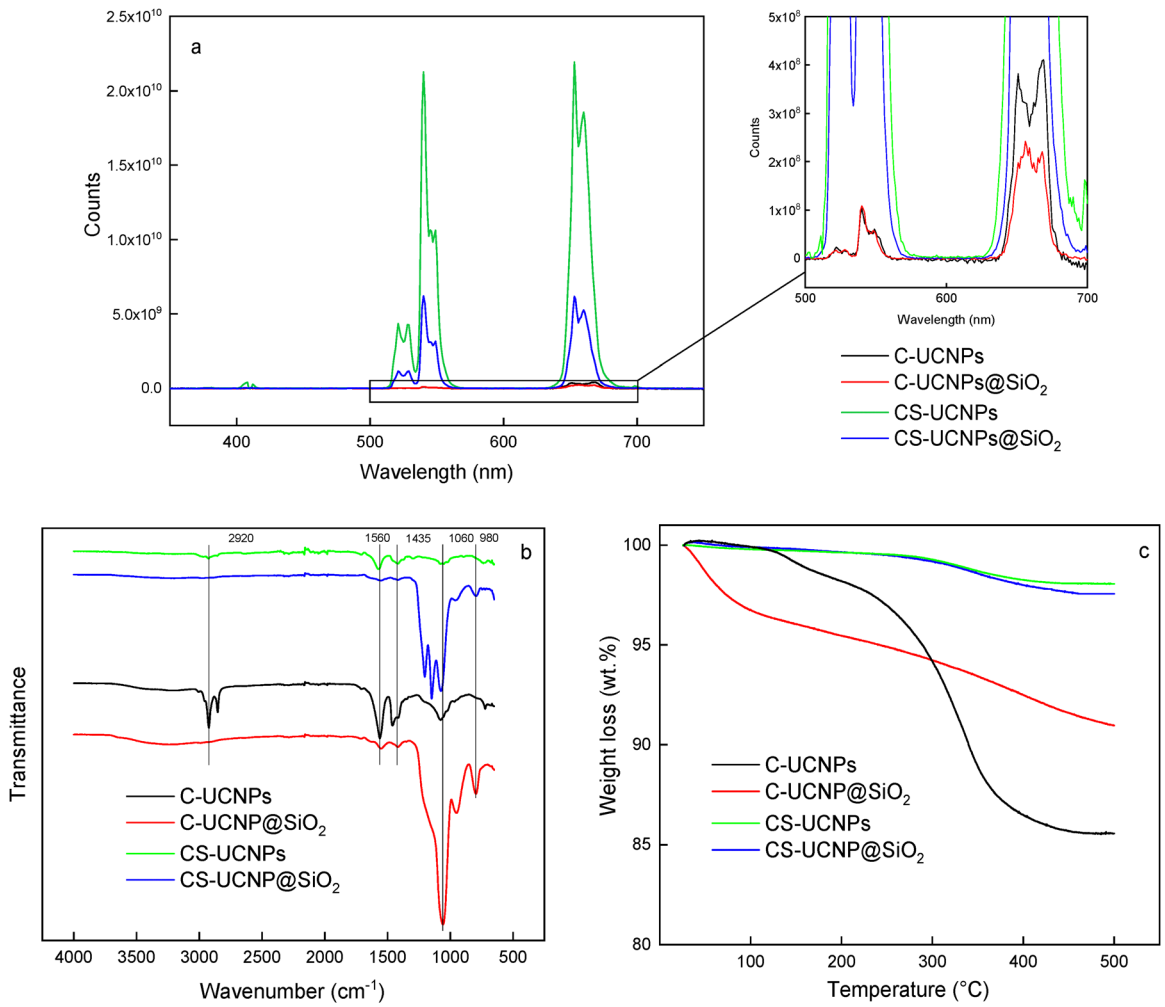

Fig. 5 (a) Fluorescence emission spectra after 980 nm excitation (the inset shows the spectra at higher magnification), (b) ATR FTIR spectra and (c) thermogravimetric analysis of C-UCNPs, C-UCNP@SiO_2, CS-UCNPs, and CS-UCNP@SiO_2 nanoparticles.

C-UCNP@SiO_2 nanoparticles confirmed the successful formation of a silica layer around the particles with a thickness of ~6.5 nm (Fig. 4b); this silica thickness was found also on CS-UCNPs. DLS measurements revealed a significant increase in the D_h of C-UCNP@SiO_2 and CS-UCNP@SiO_2 nanoparticles compared to uncoated ones. The uncoated C-UCNPs and CS-UCNPs in hexane had D_h = 19 and 66 nm, respectively, while the C-UCNP@SiO_2 and CS-UCNP@SiO_2 nanoparticles in water showed a relatively low *PD* = 0.16–0.20 with an increased D_h reaching 82 and 218 nm, respectively. This increase can be attributed to several factors: the silica shell on the nanoparticles, the hydrophilicity of the silica forming the hydration layer and the diffusion behavior of the particles in water. The relatively small D_h of the C-UCNP@SiO_2 particles indicated reduced aggregation compared to the C-UCNPs. At the same time, the ζ-potential of both C-UCNP@SiO_2 and CS-UCNP@SiO_2

nanoparticles in water decreased from +37 mV (C-UCNPs) to −23 mV (Table 2); the negative value was due to deprotonation of silanol groups. ATR FTIR spectra of C-UCNPs and C-UCNP@SiO_2 particles confirmed the removal of excessive OA from their surface and the modification by silica (Fig. 5b). The O–H and C–H stretching vibration in the range of 3000–3660 cm^{-1} and at 2920, 1560, and 1435 cm^{-1}, respectively, corresponded to residual OA bound to the C-UCNP and CS-UCNP surface. The silica modification was then evidenced by a peak at 1060 cm^{-1} ascribed to Si–O–Si bonding.

The TGA of C-UCNPs, C-UCNP@SiO_2, CS-UCNPs, and CS-UCNP@SiO_2 nanoparticles illustrated their weight loss as a function of temperature (Fig. 5c). The weight loss of C-UCNPs (15 wt%) starting from ∼100 °C and accelerating between 300–500 °C was due to the evaporation of surface adsorbed water and excessive OA. A similar trend was observed for C-UCNP@SiO_2, but with a smaller overall weight loss (9 wt%) due to the protective effect of the silica coating which prevented the degradation. Also, CS-UCNPs exhibited excellent thermal stability and minimal weight loss (2 wt%) up to 500 °C, confirming the structural integrity of the core–shell structure. Thus, the TGA results confirmed that the core–shell structure was more heat resistant than the core-only particles and that the silica coating enhanced the thermal stability.

Luminescence spectra were recorded after 980 nm excitation for all synthesized nanoparticles, namely C-UCNPs, C-UCNP@SiO_2, CS-UCNPs, and CS-UCNP@SiO_2 (Fig. 5a). The bands were ascribed to the transition of the f-electrons of Yb^{3+} ions from the ground $^2F_{7/2}$ state to the excited $^2F_{5/2}$ state. Due to the proximity of the energy levels of Yb^{3+} and Er^{3+} ions, energy could be transferred from the excited Yb^{3+} to the Er^{3+} emitter. This process led to two possible consequences: (*i*) absorption of the excitation state, where the Er^{3+} energy levels ($^2H_{11/2}$ and $^4S_{3/2}$) are pumped with energy, and (*ii*) cross-relaxation of Er^{3+} ions to the $^4F_{9/2}$ energy level. The fluorescence spectra thus showed green emission characterized by peaks at 515–534 nm and 534–560 nm, corresponding to the transitions from $^2H_{11/2}$ → $^4I_{15/2}$ and $^4S_{3/2}$ → $^4I_{15/2}$, respectively. A red emission peak at 640–674 nm was attributed to the $^4F_{9/2}$ → $^4I_{15/2}$ transition and a relatively weak blue emission was centered at ∼402–412 nm. The emission intensities of C-UCNPs and C-UCNP@SiO_2 particles at a concentration of 1 mg mL^{-1} in the 515–560 nm range were almost identical, whereas the intensity of the red emission peak (660–690 nm) of SiO_2-coated particles decreased significantly (1.7 times). This decrease can be attributed to the absorption of red light by the silica coating in the 650–670 nm region,[50] although the SiO_2 coating should be optically transparent.[15] The intensity of the emission peak of CS-UCNPs was an order of magnitude higher (170 times) than that of C-UCNPs (Fig. 5a), which is higher than the results reported in the literature.[51,52] This enhanced brightness primarily resulted from the increased energy transfer efficiency and suppression of non-radiative losses facilitated by the shell. The shell served as a protective barrier, mitigating surface quenching and preventing detrimental interactions that would otherwise lead to energy dissipation. In addition, by passivating surface defects, the shell effectively reduced non-radiative decay pathways, ensuring that a greater proportion of the absorbed energy was converted into luminescence.[51] Moreover, the shell played a key role in minimizing the cross-relaxation losses that typically occur when activating ions near the nanoparticle surface undergo inefficient energy transfer.

Cytotoxicity of nanoparticles

For *in vitro* experiments, INS-1E cells were selected as a model of insulin producing β-cells, which play a crucial role in maintaining blood glucose levels in the human body. In addition, after an eventual transplantation of Langerhans islets, quantification (imaging) of β-cells is important to evaluate the efficacy of diabetes treatment.

When studying the interactions of UCNPs with the cells, the first step was to establish their *in vitro* safety. The cytotoxicity of ultrasmall C-UCNPs was monitored using a trypan blue exclusion test based on cell counting and the fact that viable cells do not pass polar trypan blue, whereas dead cells are readily penetrated by the dye and stained. The viability of INS-1E cells incubated with C-UCNPs for 24 h reached >95% (Fig. 6). Even a high particle concentration (0.4 mg mL^{-1}) did not induce cytotoxicity, similar to PEG-neridronate-modified $NaYF_4$:Gd,Yb,Tm@$NaGdF_4$ core–shell UCNPs.[53] The fact that C-UCNPs interacted well with cells, internalized and did not damage them indicated their good biocompatibility. In this context, the biocompatibility of C-UCNPs was obviously better compared to previously investigated $NaYF_4$:Yb,Er@SiO_2-NH_2 nanoparticles, which reduced the viability of HeLa cells to 40% of control at a concentration of 0.5 mg mL^{-1}.[54] As expected, neither the silica shell of both C- and CS-UCNPs reduced cell viability.

Luminescence of nanoparticles incubated with INS-1E cells

The upconversion luminescence of C-UCNPs, CS-UCNPs, C-UCNP@SiO_2, and CS-UCNP@SiO_2 nanoparticles incubated with INS-1E cells for 24 h was monitored using a confocal microscope at 980 nm excitation (Fig. 7). Confocal micrograph showed that the nanoparticles emitted upconversion luminescence, whose spectra showed typical peaks of UCNPs at 540 and

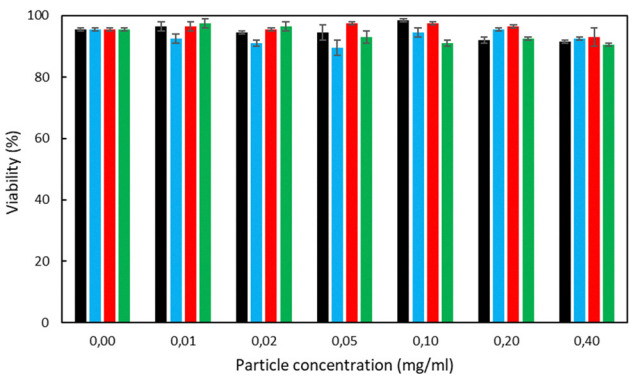

Fig. 6 Concentration-dependent viability of INS-1E cells incubated with C-UCNPs (black), C-UCNP@SiO_2 (blue), CS-UCNPs (red), and CS-UCNP@SiO_2 nanoparticles (green) for 24 h.

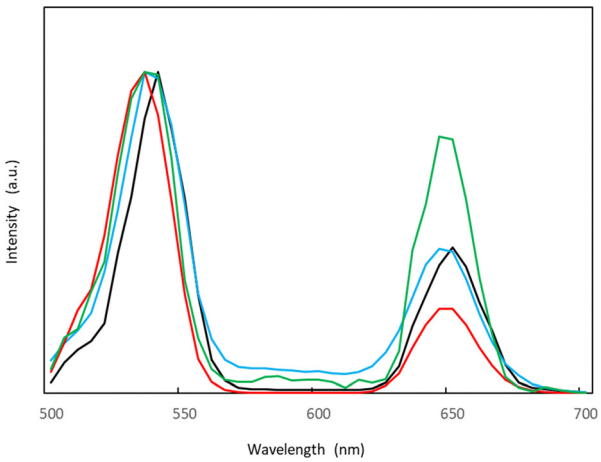

Fig. 7 Upconversion emission spectra of C-UCNPs (black), C-UCNP@SiO_2 (blue), CS-UCNPs (red), and CS-UCNP@SiO_2 nanoparticles (green) incubated with INS-1E cells for 24 h after excitation at 980 nm.

650 nm, similar to the spectrofluorometer measurements (Fig. 5a). However, the luminescence intensities of the particles incubated with INS-1E cells differed from those of the particles themselves. This was due to the fact that in the former case it was not possible to ensure the same amount of nanoparticles in the field of view, so this measurement is not suitable for comparing intensities. Even if the initial concentration of the nanoparticles was the same, it depended on their accumulation in the cells and whether they aggregated there. Accordingly, the CS-UCNPs showed the lowest luminescence intensity, as they did not penetrate the cells well and thus were the sparsely present.

After 24-h incubation of C- and CS-UCNPs and their silica-coated counterparts with INS-1E cells, the particles passively penetrated and accumulated in the cells, as documented by overlay of bright-field images of the cells with micrographs of the particles at 980 nm excitation and 530 and 640 nm emission (Fig. 8). Both the ultrasmall C-UCNPs (Fig. 8a and e) and the larger UCNP@SiO_2 nanoparticles seemed to penetrate well into the cells and in the latter case accumulated there due to the SiO_2 coating (Fig. 8b and f), similar to the CS-UCNP@SiO_2 particles (Fig. 8d and h). In contrast, the larger CS-UCNPs (without SiO_2 coating) did not penetrate much into the cells (Fig. 8c and g). At the same time, it should be noted that these experiments with all four types of nanoparticles did not result in any cell damage similar to the cell viability tests (Fig. 6).

Conclusions

Morphology and crystal structure are the most important physical parameters of UCNPs in terms of their luminescence, biocompatibility and bioavailability. Particle size influences the blood circulation lifetime, distribution in organs and clearance from the body. In this respect, ultrasmall UCNPs designed in this report are particularly advantageous as they are supposed to circulate in the body largely undetected by the immune system and, being below the renal clearance threshold, can be easily excreted in the urine. These nanoparticles were prepared in an autoclave using a new innovative method based on controlled high-temperature coprecipitation of lanthanide chlorides in the presence of water under increased pressure (2.1 MPa). The resulting nanoparticles were monodisperse and therefore had the same physical and optical properties, which provide better efficacy in bioapplications than polydisperse particles. In terms of crystal structure, hexagonal β-phase is generally preferred as it affords higher upconversion luminescence compared to other crystalline modifications. However, the spherical structure of our ultrasmall cubic α-phase UCNPs also provided sufficient luminescence. To increase luminescence, an inert $NaYF_4$ shell was epitaxially grown on the core UCNPs. The substantial

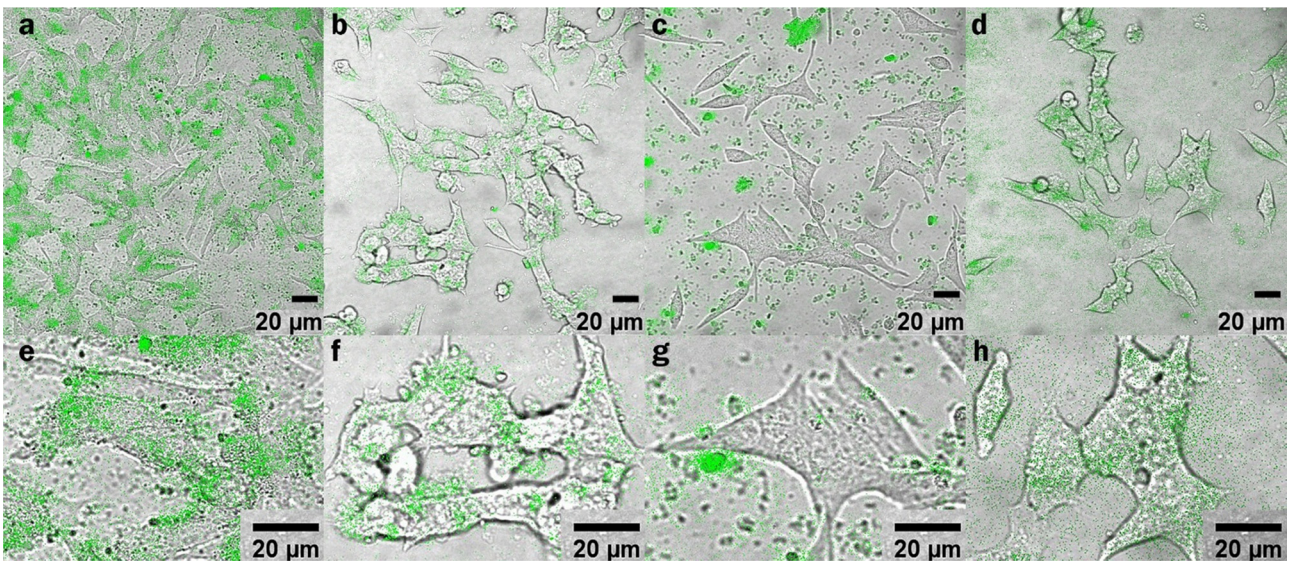

Fig. 8 Merged confocal micrographs of (a) and (e) C-UCNPs, (b) and (f) C-UCNP@SiO_2, (c) and (g) CS-UCNPs, and (d) and (h) CS-UCNP@SiO_2 nanoparticles (green) and bright-field optical images of INS-1E cells incubated for 24 h at 980 nm excitation and emission at 533 and 650 nm.

enhancement (170 times) in luminescence efficiency of CS-UCNPs was attributed to the minimization of surface quenching effects by the protective outer shell. Subsequently, the C- and CS-UCNPs were coated with silica to enhance their colloidal stability in aqueous environment and possibly to provide reactive functional groups for future bioconjugation. Coating the CS-UCNPs with silica increased the thermal stability of the nanoparticles. It was found that all UCNPs, even at a high concentration of 0.4 mg mL^{-1}, were non-cytotoxic after 24-h incubation with INS-1E cells. Ultrasmall nanoparticles (C-UCNPs) and larger C-UCNP@SiO_2 and CS-UCNP@SiO_2 particles accumulated well in cells confirming positive effect of SiO_2 coating on particle internalization. This allows the particles to be used for non-invasive diagnostic applications in medical bioimaging of diseased organs of the human body, as well as for targeted drug delivery to affected tissues.

Author contributions

MN conceived the study, designed and performed the experiments, DH wrote the manuscript. MŠ performed and analysed TEM experiments, MS performed and analysed WAXS experiments, OS interpreted fluorescence emission spectra, HE performed cell experiments and PJ interpreted biological experiments.

Conflicts of interest

There are no conflicts to declare.

Data availability

Data supporting the results of this study are available from the corresponding author upon reasonable request.

Acknowledgements

Support of the Czech Science Foundation (No. 24-10125S) is acknowledged. We would like to thank Jiřina Hromádková for electron microscopy and Prof. Petra Pullmannová from the Charles University, Faculty of Pharmacy for the SWAXS measurements.

References

1 S. Borse, R. Rafique, Z. V. P. Murthy, T. J. Park and S. K. Kailasa, Applications of upconversion nanoparticles in analytical and biomedical sciences: A review, *Analyst*, 2022, **147**, 3155–3179, DOI: **10.1039/D1AN02170B**.

2 Z. Xiaohui, Z. Jing, L. Jinliang and Z. Yong, Recent progress of rare-earth doped upconversion nanoparticles: Synthesis, optimization, and applications, *Adv. Sci.*, 2019, **6**, 1901358–1901388, DOI: **10.1002/advs.201901358**.

3 F. Hu, Z. Ye, A. Pickel and W. Tenhaeff, Operando characterization of lithium battery internal temperatures via upconverting nanoparticle thermometry, *Nanoscale*, 2025, **17**, 14597–14606, DOI: **10.1039/d5nr01160d**.

4 Y. Zhong, I. Rostami, Z. Wang, H. Dai and Z. Hu, Energy migration engineering of bright rare-earth upconversion nanoparticles for excitation by light-emitting diodes, *Adv. Mater.*, 2015, **27**, 6418–6422, DOI: **10.1002/adma.201502272**.

5 B. Richards, D. Hudry, D. Busko, A. Turshatov and I. A. Howard, Photon upconversion for photovoltaics and photocatalysis: A critical review, *Chem. Rev.*, 2021, **121**, 9165–9195, DOI: **10.1021/acs.chemrev.1c00034**.

6 J. Gonçalves, A. Bastos, S. Ribeiro, L. Carlos, R. Longo, J. Caiut and R. Ferreira, Thermal properties of nanofluids using hydrophilic and hydrophobic $LiYF_4$:Yb/Er upconverting nanoparticles, *Nanoscale Adv.*, 2024, **6**, 1486–1496, DOI: **10.1039/d3na01114c**.

7 H. Suo, Q. Zhu, X. Zhang, B. Chen, J. Chen and F. Wang, High-security anti-counterfeiting through upconversion luminescence, *Mater. Today Phys.*, 2021, **21**, 100520, DOI: **10.1016/j.mtphys.2021.10052**.

8 P. Zhang, L. Liang and X. Liu, Lanthanide-doped nanoparticles in photovoltaics – more than just upconversion, *J. Mater. Chem. C*, 2021, **9**, 16110–16131, DOI: **10.1039/D1TC02441H**.

9 M. Alkahtani, A. Almuqhim, H. Qasem, N. Alsofyani, A. Alfahd, S. Alenzi, A. Aljuwayr, Y. Alzahrani, A. Al-Badri and M. Alotaibi, Lithium-based upconversion nanoparticles for high performance perovskite solar cells, *Nanomaterials*, 2021, **11**, 2909, DOI: **10.3390/nano11112909**.

10 W. Wu, J. Yu, S. Dong and J. Hao, Photovoltaic energy conversion and storage of micro-supercapacitors based on emulsion self-assembly of upconverting nanoparticles, *ACS Cent. Sci.*, 2021, **7**, 1611–1621, DOI: **10.1021/acscentsci.1c00795**.

11 P. Jethva, M. Momin, T. Khan and A. Omri, Lanthanide-doped upconversion luminescent nanoparticles-evolving role in bioimaging, biosensing, and drug delivery, *Materials*, 2022, **15**, 2374, DOI: **10.3390/ma15072374**.

12 Z. Gu, L. Yan, G. Tian, S. Li, Z. Chai and Y. Zhao, Recent advances in design and fabrication of upconversion nanoparticles and their safe theranostic applications, *Adv. Mater.*, 2013, **25**, 3758–3779, DOI: **10.1002/adma.201301197**.

13 S. H. Nam, Y. M. Bae, Y. I. Park, J. H. Kim, H. M. Kim, J. S. Choi, K. T. Lee, T. Hyeon and Y. D. Suh, Long-term real-time tracking of lanthanide ion doped upconverting nanoparticles in living cells, *Angew. Chem., Int. Ed.*, 2011, **50**, 6093–6097, DOI: **10.1002/anie.201007979**.

14 C. Wang, L. Cheng and Z. Liu, Upconversion nanoparticles for photodynamic therapy and other cancer therapeutics, *Theranostics*, 2013, **3**, 317–330, DOI: **10.7150/thno.5284**.

15 A. Hlaváček, Z. Farka, M. J. Mickert, U. Kostiv, J. C. Brandmeier, D. Horák, P. Skládal, F. Foret and H. H. Gorris, Bioconjugates of photon-upconversion nanoparticles for cancer biomarker detection and imaging, *Nat. Protoc.*, 2022, **17**, 1028–1072, DOI: **10.1038/s41596-021-00670-7**.

16 O. Shapoval, J. C. Brandmeier, M. Nahorniak, V. Oleksa, E. Makhneva, H. H. Gorris, Z. Farka and D. Horák, PMVEMA-coated upconverting nanoparticles for upconversion-linked immunoassay of cardiac troponin, *Talanta*, 2022, **244**, 123400, DOI: **10.1016/j.talanta.2022.123400**.

17 T. Vasylyshyn, V. Patsula, D. Větvička, O. Shapoval, J. Pankrác, M. Kabešová, J. Benešb and D. Horák, Intraperitoneal versus intravenous administration of Flamma®-conjugated PEG-alendronate-coated upconversion nanoparticles in a mouse pancreatic cancer model, *Nanoscale Adv.*, 2025, **7**, 144–154, DOI: **10.1039/D4NA00764F**.

18 A. Bednarkiewicz, M. Szalkowski, M. Majak, Z. Korczak, M. Misiak and S. Maćkowski, All-optical data processing with photon-avalanching nanocrystalline photonic synapse, *Adv. Mater.*, 2023, **35**, e2304390, DOI: **10.1002/adma.202304390**.

19 Q. Q. Dou and Y. Zhang, Tuning of the structure and emission spectra of upconversion nanocrystals by alkali ion doping, *Langmuir*, 2011, **27**, 13236–13241, DOI: **10.1021/la201910t**.

20 D. LI, Q. Shao, Y. Dong and J. Jiang, Phase-, shape- and size-controlled synthesis of $NaYF_4$:Yb^{3+}, Er^{3+} nanoparticles using rare-earth acetate precursors, *J. Rare Earths*, 2014, **32**, 1032–1036, DOI: **10.1016/S1002-0721(14)60179-4**.

21 M. Wang, G. Abbineni, A. Clevenger, C. Mao and S. Xu, Upconversion nanoparticles: Synthesis, surface modification and biological applications, *Nanomed.: Nanotechnol. Biol. Med.*, 2011, **7**, 710–729, DOI: **10.1016/j.nano.2011.02.013**.

22 G. Chen, H. Qiu, P. N. Prasad and X. Chen, Upconversion nanoparticles: Design, nanochemistry, and applications in theranostics, *Chem. Rev.*, 2014, **114**, 5161–5214, DOI: **10.1021/cr400425h**.

23 S. Fischer, R. D. Mehlenbacher, A. Lay, C. Siefe, A. P. Alivisatos and J. A. Dionne, Small alkaline-earth-based core/shell nanoparticles for efficient upconversion, *Nano Lett.*, 2019, **19**, 3878–3885, DOI: **10.1021/acs.nanolett.9b01057**.

24 Y. Jiao, C. Ling, J.-X. Wang, H. Amanico, J. Saczek, H. Wang, S. Sridhar, B. B. Xu, S. Wang and D. Wang, Controllable synthesis of upconversion nanophosphors toward scale-up productions, *Part. Part. Syst. Charact.*, 2020, **37**, 2000129, DOI: **10.1002/ppsc.202000129**.

25 T. Ho, S. Hong, C. Yang, Y. Chen, H. Lin and T. Wang, Preparation of green emission and red emission ligand-free upconverting nanoparticles for investigation of the generation of reactive oxygen species applied to photodynamic therapy, *J. Alloys Compd.*, 2022, **10**, 162323, DOI: **10.1016/j.jallcom.2021.162323**.

26 A. Schroter, S. Märkl, N. Weitzel and T. Hirsch, Upconversion nanocrystals with high lanthanide content: Luminescence loss by energy migration versus luminescence enhancement by increased NIR absorption, *Adv. Funct. Mater.*, 2022, **32**, 2113065, DOI: **10.1002/adfm.202113065**.

27 O. Shapoval, H. Engstová, D. Jirák, J. Drahokoupil, K. Sulková, O. Pop-Georgievski, P. Ježek and D. Horák, Poly(4-styrenesulfonic acid-*co*-maleic anhydride)-coated $NaGdF_4$:Yb,Tb,Nd nanoparticles with luminescent and magnetic properties for pancreatic β-cell and Langerhans islet imaging, *ACS Appl. Mater. Interfaces*, 2022, **14**, 18233–18247, DOI: **10.1021/acsami.2c04274**.

28 T. Joshi, C. Mamat and H. Stephan, Contemporary synthesis of ultrasmall (sub-10 nm) upconverting nanomaterials, *ChemistryOpen*, 2020, **9**, 703–712, DOI: **10.1002/open.202000073**.

29 I. Halimi, E. M. Rodrigues, S. L. Maurizio, H.-Q. T. Sun, M. Grewal, E. M. Boase, N. Liu, R. Marin and E. Hemmer, Pick your precursor! Tailoring the size and crystal phase of microwave-synthesized sub-10 nm upconverting nanoparticles, *J. Mater. Chem. C*, 2019, **7**, 15364–15374, DOI: **10.1039/C9TC04817K**.

30 D. Mendez-Gonzalez, V. T. Vera, I. Z. Gutierrez, C. Gerke, C. Cascales, J. Rubio-Retama, O. G. Calderón, S. Melle and M. Laurenti, Upconverting nanoparticles in aqueous media: Not a dead-end road. Avoiding degradation by using hydrophobic polymer shells, *Small*, 2022, **18**, 2105652, DOI: **10.1002/smll.202105652**.

31 O. Dukhno, F. Przybilla, V. Muhr, M. Buchner, T. Hirsch and Y. Mély, Time-dependent luminescence loss of individual upconversion nanoparticles upon dilution in aqueous solutions, *Nanoscale*, 2018, **10**, 15904–15910, DOI: **10.1039/C8NR03892A**.

32 L. Wang, Y. Zhang and Y. Zhu, One-pot synthesis and strong near-infrared upconversion luminescence of poly(acrylic acid)-functionalized YF_3:Yb^{3+}/Er^{3+} nanocrystals, *Nano Res.*, 2010, **3**, 317–325, DOI: **10.1007/s12274-010-1035-z**.

33 C. Homann, E. M. Rodrigues, P. Orsini, K. Savard, C. B. Togola, M. M. Denus-Baillargeon, M. Massabki and E. Hemmer, Gum Arabic-stabilized upconverting nanoparticles for printing applications, *Opt. Mater.: X*, 2024, **21**, 100290, DOI: **10.1016/j.omx.2024.100290**.

34 V. Bastos, P. Oskoei, E. Andresen, M. I. Saleh, B. Rühle, U. Resch-Genger and H. Oliveira, Stability, dissolution, and cytotoxicity of $NaYF_4$-upconversion nanoparticles with different coatings, *Sci. Rep.*, 2022, **12**, 3770, DOI: **10.1038/s41598-022-07630-5**.

35 U. Kostiv, Z. Farka, M. J. Mickert, H. H. Gorris, N. Velychkivska, O. Pop-Georgievski, M. Pastucha, E. Odstrčilíková, P. Skládal and D. Horák, Versatile bioconjugation strategies of PEG-modified upconversion nanoparticles for bioanalytical applications, *Biomacromolecules*, 2020, **21**, 4502–4513, DOI: **10.1021/acs.biomac.0c00459**.

36 H. Zhang, X. Wang, R. Jin and Q. Su, Preparation and applications of polymer-modified lanthanide-doped upconversion nanoparticles, *Giant*, 2022, **12**, 100130, DOI: **10.1016/j.giant.2022.100130**.

37 I. A. Khan, T. Yu, M. Yang, J. Liu and Z. Chen, A systematic review of toxicity, biodistribution, and biosafety in upconversion nanomaterials: Critical insights into toxicity mitigation strategies and future directions for safe applications, *BME Front.*, 2025, **6**, 0120, DOI: **10.34133/bmef.0120**.

38 C. Liu, S. Sun and J. Mao, Water-soluble Yb^{3+}, Er^{3+} codoped $NaYF_4$ nanoparticles induced SGC-7901 cell apoptosis through mitochondrial dysfunction and ROS-mediated ER stress, *Hum. Exp. Toxicol.*, 2023, **42**, 9603271231188493, DOI: **10.1177/09603271231188493**.

39 Y. Huang, P. Li, R. Zhao, L. Zhao, J. Liu, S. Peng, X. Fu, X. Wang, R. Luo, R. Wang and Z. Zhang, Silica nanoparticles: Biomedical applications and toxicity, *Biomed. Pharmacother.*, 2022, **151**, 113053, DOI: **10.1016/j.biopha.2022.113053**.

40 M. Nahorniak, O. Pop-Georgievski, N. Velychkivska, M. Filipová, E. Rydvalová, K. Gunár, P. Matouš, U. Kostiv and D. Horák, Rose Bengal-modified upconverting nanoparticles: Synthesis, characterization, and biological evaluation, *Life*, 2022, **12**, 1383, DOI: **10.3390/life12091383**.

41 M. Świętek, Y.-H. Ma, N.-P. Wu, A. Paruzel, W. Tokarz and D. Horák, Tannic acid coating augments glioblastoma cellular uptake of magnetic nanoparticles with antioxidant effects, *Nanomaterials*, 2022, **12**, 1310, DOI: **10.3390/nano12081310**.

42 O. Shapoval, V. Oleksa, M. Šlouf, V. Lobaz, O. Trhlíková, M. Filipová, O. Janoušková, H. Engstová, J. Pankrác, A. Modrý, V. Herynek, P. Ježek, L. Šefc and D. Horák, Colloidally stable P(DMA-AGME)-Ale-coated Gd(Tb)F_3:Tb^{3+}(Gd^{3+}),Yb^{3+},Nd^{3+} nanoparticles as a multimodal contrast agent for down- and upconversion luminescence, magnetic resonance imaging, and computed tomography, *Nanomaterials*, 2021, **11**, 230, DOI: **10.3390/nano11010230**.

43 Program package EDIFF, **https://pypi.org/project/ediff**.

44 L. Glasser, Crystallographic Information Resources, *J. Chem. Educ.*, 2016, **93**, 542–549, DOI: **10.1021/acs.jchemed.5b00253**.

45 M. Asfari, D. Janjic, P. Meda, G. Li, P. A. Halban and C. B. Wollheim, Establishment of 2-mercaptoethanol-dependent differentiated insulin-secreting cell lines, *Endocrinology*, 1992, **130**, 167–178, DOI: **10.1210/endo.130.1.1370150**.

46 J. Tanmaya, M. Constantin and S. Holger, Contemporary synthesis of ultrasmall (sub-10 nm) upconverting nanomaterials, *ChemistryOpen*, 2020, **9**, 703–712, DOI: **10.1002/open.202000073**.

47 H. Cui, Y. Feng, W. Ren, T. Zeng, H. Lv and Y. Pan, Strategies of large scale synthesis of monodisperse nanoparticles, *Recent Pat. Nanotechnol.*, 2009, **3**, 32–41, DOI: **10.2174/187221009787003302**.

48 J. Kim and D. F. Lawler, Characteristics of zeta potential distribution in silica particles, *Bull. Korean Chem. Soc.*, 2005, **26**, 1083–1089, DOI: **10.5012/bkcs.2005.26.7.1083**.

49 X. Chen, D. Peng, Q. Ju and F. Wang, Photon upconversion in core-shell nanoparticles, *Chem. Soc. Rev.*, 2015, **44**, 1318–1330, DOI: **10.1039/c4cs00151f**.

50 W. Suthabanditpong, R. Buntem, C. Takai, M. Fuji and T. Shirai, The quantitative effect of silica nanoparticles on optical properties of thin solid silica UV-cured films, *Surf. Coat. Technol.*, 2015, **279**, 25–31, DOI: **10.1016/j.surfcoat.2015.07.068**.

51 S. Fischer, N. Johnson, J. Pichaandi, J. C. Goldschmidt and F. van Veggel, Upconverting core-shell nanocrystals with high quantum yield under low irradiance: On the role of isotropic and thick shells, *J. Appl. Phys.*, 2015, **118**, 193105, DOI: **10.1063/1.4936119**.

52 S. Wilhelm, Perspectives for upconverting nanoparticles, *ACS Nano*, 2017, **11**, 10644–10653, DOI: **10.1021/acsnano.7b07120**.

53 U. Kostiv, M. M. Natile, D. Jirák, D. Půlpánová, K. Jiráková, M. Vosmanská and D. Horák, PEG-neridronate-modified $NaYF_4$:Gd^{3+},Yb^{3+},Tm^{3+}/$NaGdF_4$ core-shell upconverting nanoparticles for bimodal magnetic resonance/optical luminescence imaging, *ACS Omega*, 2021, **6**, 14420–14429, DOI: **10.1021/acsomega.1c01313**.

54 U. Kostiv, O. Janoušková, M. Šlouf, N. Kotov, H. Engstová, K. Smolková, P. Ježek and D. Horák, Silica-modified monodisperse hexagonal lanthanide nanocrystals: Synthesis and biological properties, *Nanoscale*, 2015, **7**, 18096–18104, DOI: **10.1039/C5NR05572E**.